PLEASE CITE THIS ARTICLE AS DOI: 10.1063/5.0146305

Jianming Cui, ¹ Saksham Phul, ¹ and Kristen A. Fichthorn ^{1,2,*} Department of Chemical Engineering¹ and Department of Physics² The Pennsylvania State University University Park, PA 16802 USA

*Corresponding Author: fichthorn@psu.edu

Crystals with penta-twinned structures can be produced from diverse fcc metals, but the mechanisms that control the final product shapes are still not well understood. Using the theory of absorbing Markov chains to account for the growth of penta-twinned decahedral seeds via atom deposition and surface diffusion, we predicted the formation of various types of products: decahedra, nanorods, and nanowires. We showed that the type of product depends on the morphology of the seed and that small differences between various seed morphologies can lead to significantly different products. For the case of uncapped Dh seeds, we compared predictions from our model to nanowire morphologies obtained in two different experiments and obtained favorable agreement. Possible extensions of our model are indicated.

PLEASE CITE THIS ARTICLE AS DOI: 10.1063/5.0146305

INTRODUCTION

Penta-twinned nanocrystals can be produced from diverse fcc metals.¹⁻²⁷ Various penta-twinned nanocrystal shapes can be synthesized, including nanowires (NW),¹⁻¹⁴ nanorods (NR),^{3, 5, 10, 15-18} and various types of decahedra (Dh).^{10, 19-26} Penta-twinned NWs can be applied as efficient as electrocatalysts,²⁸ in wearable electronic textiles,²⁹ photothermal desalination,³⁰ in thin films for electromagnetic interference shielding,³¹ electrochromic devices,³²⁻³⁴ low-voltage electrical heaters,³⁵ and flexible, transparent, conductive films for many applications.³⁶⁻⁴⁰ Gold NR have promising applications in photothermal theraputics and drug delivery.^{41, 42} Dh have shown favorable performance as catalysts,⁴³ nanoresonators for surface enhanced Raman scattering,⁴⁴ and sensors.⁴⁵

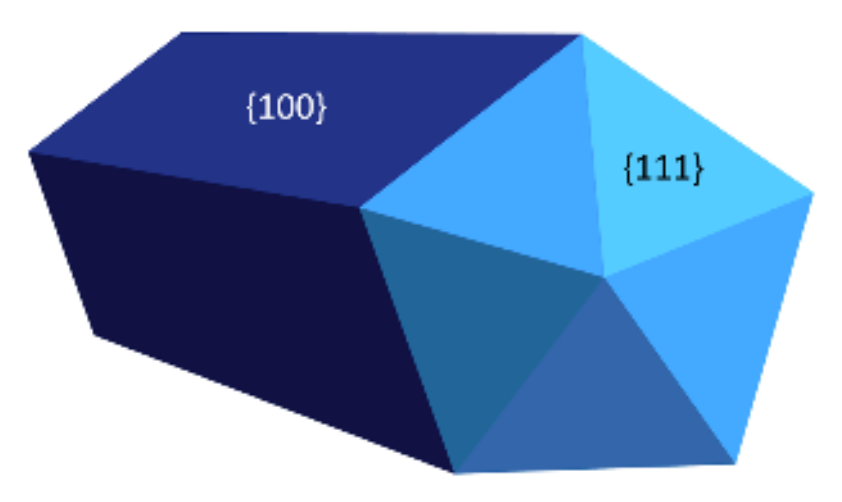


Figure 1. Schematic showing the major features of a penta-twinned NW. {111} "end" facets are shown in lighter shades of blue and {100} "side" facets are shown in dark blue.

Figure 1 shows a schematic of the major features of a penta-twinned NW, which has 10 {111} "end" facets, five on each end, and five{100} "side" facets. In this work, we define a NW as having an aspect ratio (ratio of the end-to-end length to the width) of ten or greater. If we reduce the {100} length so the aspect ratio is between one and 10, we

PLEASE CITE THIS ARTICLE AS DOI: 10.1063/5.0146305

Kinetic shapes for penta-twinned nanocrystals can emerge either through aggregative mechanisms⁵¹⁻⁵⁵ or they can grow from seeds through a combination of atom deposition and nanocrystal reshaping driven by surface diffusion.⁵⁴ In this paper, we consider the growth of a Dh nanocrystal seed *via* atom deposition and surface diffusion. We use the theory of absorbing Markov chains to describe atom diffusion between the crystal facets. Our work is complementary to recent work by El Koraychy *et al.*⁵⁶ They used molecular dynamics (MD) simulations to study how Dh and icosahedral seed crystals evolve from the growth of tetrahedra, where the largest crystals in their study were roughly on the 6 nm scale.⁵⁶ Here, we examine the growth Dh with diameters ranging from 6-60 nm. We show that the final growth morphology can be highly sensitive to the initial Dh seed geometry and lead to Dh, NR, or NW, depending on the structure of the seed.

Background

In previous studies, we developed a kinetic growth model for penta-twinned Ag and Cu NWs considering that the growth of a particular facet is driven by a competition between atom deposition and inter-facet diffusion of deposited atoms.⁵⁷⁻⁵⁹ In this model, growth begins from a Dh penta-twinned seed crystal consisting of two primary facets, $\{111\}$ and $\{100\}$. Atoms are assumed to be randomly deposited and deposited atoms can diffuse between and accumulate on the facets. The growth rate G_i of a particular facet i is

This is the author's peer reviewed, accepted manuscript. However, the online version of record will be different from this version once it has been copyedited and typeset.

PLEASE CITE THIS ARTICLE AS DOI: 10.1063/5.0146305

equal to the accumulation rate of atoms on facet i, so for two types of facets ({111} and {100}) we have,

$$G_{\{111\}} = R_{dep,\{111\}} + R_{\{100\} \to \{111\}} - R_{\{111\} \to \{100\}}$$
 , (1)

and

$$G_{\{100\}} = R_{dep,\{100\}} + R_{\{111\} \to \{100\}} - R_{\{100\} \to \{111\}}$$
 (2)

Here, $R_{dep,i}$ is the deposition rate on facet *i* and $R_{i\rightarrow i}$ is the net atomic diffusion rate between facets j and i. It should be noted that the units of all the quantities in Equations (1) and (2) are reciprocal time (e.g., s⁻¹).

Depending on the relative values of the deposition and diffusion rates, various structures can be realized. For example, if the deposition rate is much faster than the inter-facet diffusion rate, then $G_{\{111\}} = R_{dep,\{111\}}, G_{\{100\}} = R_{dep,\{100\}},$ and the kinetic Wulff construction^{60, 61} can be used to predict the nanocrystal shape. Our prior studies showed that to achieve a long NW based on deposition only, the ratio of deposition rates on the {111} end and {100} side facets must be nearly equal to the NW aspect ratio.⁵⁷ However, this was not the case in at least one study where NWs were grown.¹³ In a study of the growth of Cl-capped Cu NWs, Kim et al. performed synthesis experiments, along with complementary electrochemical experiments aimed at characterizing the Cu deposition (reduction) rate. 13 Their electrochemical experiments indicated the deposition rate on Cu(111) was only 14.5 times greater than on Cu(100). This ratio was insufficient to predict the experimentally observed NW, suggesting inter-facet diffusion played a role in nanowire growth in this system.

The theoretical description of kinetic nanocrystal shapes becomes substantially more complex when inter-facet diffusion is important. Though Equations (1) and (2) are still valid,

PLEASE CITE THIS ARTICLE AS DOI: 10.1063/5.0146305

the inter-facet diffusion rates become dependent on facet size, so that the linear-facet growth rates change as a nanocrystal grows. From an atomistic perspective, atom accumulation on a facet changes the inter-facet diffusion rate because metal atoms interact strongly with one another, and these interactions affect local adatom hopping rates. Thus, the inter-facet diffusion rates become a complicated function of the atom coverage and distribution on a crystal facet when the facet is not smooth. Theoretical techniques such as kinetic Monte Carlo (kMC)⁶² can describe crystal-shape evolution under these complex conditions. If the adatom hopping rate can be quantified for each possible local environment on a crystal surface, then the kMC description is exact, or at least as accurate as one would obtain via ab initio molecular dynamics (MD) – if such a simulation could be run to arbitrarily long times.

There are situations under which kMC simulations yield the same results as differential equations and these circumstances can occur in crystal growth. For example, if accumulation occurs on one crystal facet, but not another, the atom concentration on the facet without accumulation is dilute and the adatom hopping rates are those for isolated atoms. There is at least one experimental precedent for this scenario in the Br-mediated growth of Ag nanowires, where Da Silva et al. observed that Ag nanowires maintained a constant diameter for 35 minutes, while they grew to achieve an aspect ratio of around 1000.8 Subsequent to this 35minute interval, the wire diameters began to increase. This observation indicates there was no accumulation on the sides of the nanowires while they grew longer, at least for a time. Such a scenario can be described by the theory of absorbing Markov chains. 63-67

In the theory of absorbing Markov chains, temporal evolution is based on the Master equation, where the time evolution of states is given by

$$\frac{d\vec{P}}{dt} = -A \vec{P} \tag{5}$$

PLEASE CITE THIS ARTICLE AS DOI: 10.1063/5.0146305

Here, $\vec{P} = \{P_i\}$ is the probability state i occurs at time t, and A is the transition-rate matrix. The elements of A are given by

$$A_{ij} = \begin{cases} \sum_{k} r_{ik}, & \text{if } i = j \\ -r_{ji}, & \text{if } i \neq j \end{cases}$$

$$(6)$$

where r_{ij} is the rate to transit from state i to j.

The theory of absorbing Markov chains⁶³⁻⁶⁷ can be applied to calculate the Mean First-Passage Time (MFPT) $\langle t_{i \to j} \rangle$, or the average time for an atom to transit from facet i to facet j. We note $\langle t_{i \to j} \rangle^{-1} = R_{i \to j}$ in Equations (1) and (2). To calculate the MFPT, we convert the transition-rate matrix \boldsymbol{A} into the Markov matrix \boldsymbol{M} as follows. First, we define two types of states: transient states and absorbing states. In transient states, transitions can occur to other states, while absorbing states are final states, where no further transitions occur. When we calculate $\langle t_{i \to j} \rangle$, or $R_{i \to j}$ in Equations (1) and (2), there are N_A absorbing states and N_T transient states. Based on these two types of states, we define the Markov matrix \boldsymbol{M} as

$$M = \begin{pmatrix} I & \mathbf{0} \\ R & T \end{pmatrix} \qquad , \tag{6}$$

where I is an identity matrix with dimensions of $N_A \times N_A$, $\mathbf{0}$ is a null matrix with dimensions of $N_A \times N_T$, \mathbf{R} is the recurrent matrix with dimensions of $N_T \times N_A$ and \mathbf{T} is the transient matrix with dimensions of $N_T \times N_T$. The recurrent matrix accounts for transitions between transient and absorbing states and the transient matrix contains the rates for transitions between transient states. In converting \mathbf{A} to \mathbf{M} , it is best to order the states and assign indices such that the transient states are first, followed by absorbing

PLEASE CITE THIS ARTICLE AS DOI: 10.1063/5.0146305

states, as shown in the example in the **Supplementray Information**. The elements of the transient matrix are given by

$$T_{ij} = \begin{cases} 0, & \text{if } i = j \\ r_{ij} \tau_i, & \text{if } i \neq j \end{cases}$$

$$(7)$$

and the elements of the recurrent matrix are given by

$$R_{i(j-N_T)} = r_{ij} \,\tau_i \quad , \tag{8}$$

where r_{ij} is an appropriate rate in \boldsymbol{A} [Equation (6)] and $\tau_i = A_{ii}^{-1}$. An example of constructing the Markov matrix and its various sub-matrices is given in ref. ⁶⁷ As we will discuss below, we also included an example of constructing the Markov matrix for trimer diffusion on Ag(111) in the **Supplementary Information.**

When the Markov matrix and its submatrices have been defined, the MPFT and the exit probability distribution for various absorbing states \vec{P}_{exit} can be obtained from

$$\langle t_{i \to j} \rangle = \vec{p}_0^T \cdot (\boldsymbol{I_T} - \boldsymbol{T})^{-1} \cdot \vec{\tau} \qquad , \tag{9}$$

and

$$\vec{P}_{exit} = \vec{p}_0^T \cdot (\boldsymbol{I_T} - \boldsymbol{T})^{-1} \cdot \boldsymbol{R} \qquad , \tag{10}$$

where \vec{p}_0^T is the initial probability that the transient states are occupied and I_T is an identity matrix with the same dimensions as T. As we will discuss below, we included an example of calculating the MFPT for trimer diffusion on Ag(111) in the **Supplementary** Information.

In the theory of absorbing Markov chains, we describe time evolution by enumerating every state of the system, along with all rates to transit from one state to another. This is possible in the dilute limit of a single atom (or a unit, such as a trimer) diffusing on a facet

PLEASE CITE THIS ARTICLE AS DOI: 10.1063/5.0146305

By applying the theory of absorbing Markov chains to describe the evolution of one facet, assuming accumulation occurred on another, we were able to explain experimentally observed aspect ratios for the growth of uncapped Ag nanowires,⁵⁷ Cl-covered Cu nanowires,⁵⁸ and I-covered Cu nanoplates.⁶⁸ While we predicted high aspect ratios for the capped Cu morphologies, including aspect ratios greater than 1000 for the capped Cu NWs,⁵⁸ the aspect ratios for uncapped Ag NWs were smaller, around $100.^{57}$ In the Ag study, we probed the growth of a Dh seed crystal of a single size – 28 nm. The fact that the inter-facet rates $R_{i\rightarrow j}$ in Equations (1) and (2) depend on facet size suggests that multiple shapes could be predicted, in which the growth product (NW, NR, or Dh) depends on seed dimensions.

In this paper, we explore the dependence of the growth morphology on the initial seed dimensions for the growth of uncapped Dh Ag seeds. As depicted in **Figure 2**, we show there is a set of seed morphologies for which the initial morphology leads to approximately equal growth of the length and diameter. For example, the seed shown in **Figure 2(a)**, which has a length of 8.9 nm and a diameter of 7.4 nm, is predicted to possess nearly equal growth rates of the {100} and the {111} facets, so final shape is a Dh. The seed in **Figure 2(b)** has a length of 13.5 nm and a diameter of 7.4 nm, and is predicted to grow wider, to produce a Dh. Conversely, the seed depicted in **Figure 2(c)** has a length of 13.8 nm and a diameter of 15.2

PLEASE CITE THIS ARTICLE AS DOI: 10.1063/5.0146305

nm and is predicted to grow longer, to produce a NW. In summary, below a critical initial seed width that depends on the length, seeds will grow wider and remain as Dh. Conversely, below a critical initial seed length that depends on the seed width, seeds will grow longer to produce NR and NW. Below, we describe this study.

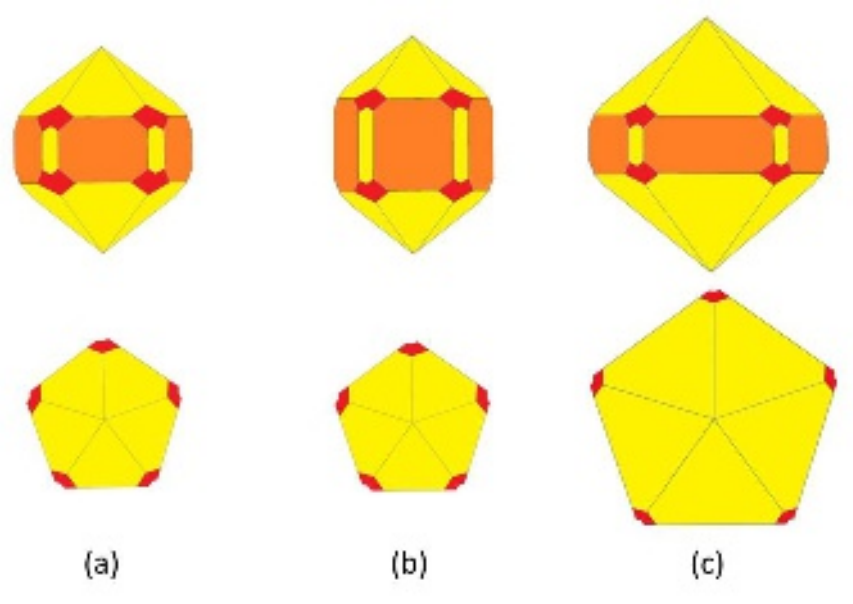


Figure 2. Overview of three types of Marks-Dh seed morphologies in this study. {111} facets are yellow, {100} facets are orange, and {110} facets are red. Both end-on and side views are shown. (a) The {100} width is 16 atoms (diameter of 7.4 nm), and the {100} length is 16 atoms, (total length of 8.9 nm), $R_{\{100\}\rightarrow\{111\}} \approx R_{\{111\}\rightarrow\{100\}}$, and the growth morphology is predicted to be a Dh. (b) The {100} width is 16 atoms, the {100} length is 32 atoms (total length of 13.5 nm), $R_{\{100\}\rightarrow\{111\}} < R_{\{111\}\rightarrow\{100\}}$, and the growth shape is predicted to be a Dh. (c) The {100} width is 32 atoms (diameter of 15.2 nm), the {100} length is 16 atoms (total length of 13.8 nm), $R_{\{100\}\rightarrow\{111\}} > R_{\{111\}\rightarrow\{100\}}$, and the growth shape is predicted to be a NW.

MODELS AND METHODS

We consider the growth of Dh Ag seeds with the geometry of a Marks Dh,⁶⁹ similar to those shown in **Figure 2**. As we see in **Figure 2**, the main facets in the Marks Dh are the {111} "end" facets and the {100} "side" facets. Additionally, the Marks Dh possesses {111} "notches" on

PLEASE CITE THIS ARTICLE AS DOI: 10.1063/5.0146305

the sides and {110} "steps" between the notches and the end facets. In this work, we create the notches by removing two layers of atoms from the {100} twin boundaries and the {110} step is three unit-cells wide. We describe Ag interatomic interactions using an Embedded-Atom Method (EAM) potential. MD simulations were run using the LAMMPS code. In prior MD simulation studies of a penta-twinned structure with a 28 nm diameter, the Marks Dh was shown to be the energetically favored structure.

To gauge the major diffusion processes involved in $R_{\{111\}\to\{100\}}$ and $R_{\{100\}\to\{111\}}$, we ran MD simulations on Ag seed crystals. The seeds were equilibrated for 4 ns in canonical MD simulations using the Nosé-Hoover thermostat at 450 K. The $\{100\}$ width of the seeds was 30 atoms (diameter of 14.21 nm) and the $\{100\}$ length was 20 atoms (total length of 14.31 nm). 15 adatoms were randomly added onto the $\{111\}$ facet for each equilibration.

We also calculated energy barriers for the diffusion processes relevant for seed growth using the climbing-image nudged-elastic band (CI-NEB) method,⁷² implemented in LAMMPS. In these calculations, the seed crystal had {100} facets with a width of 60 atoms and a length of 20 atoms. The diameter was 28.91 nm, the total length was 23.44 nm, and there were in total 347,394 atoms in this system.

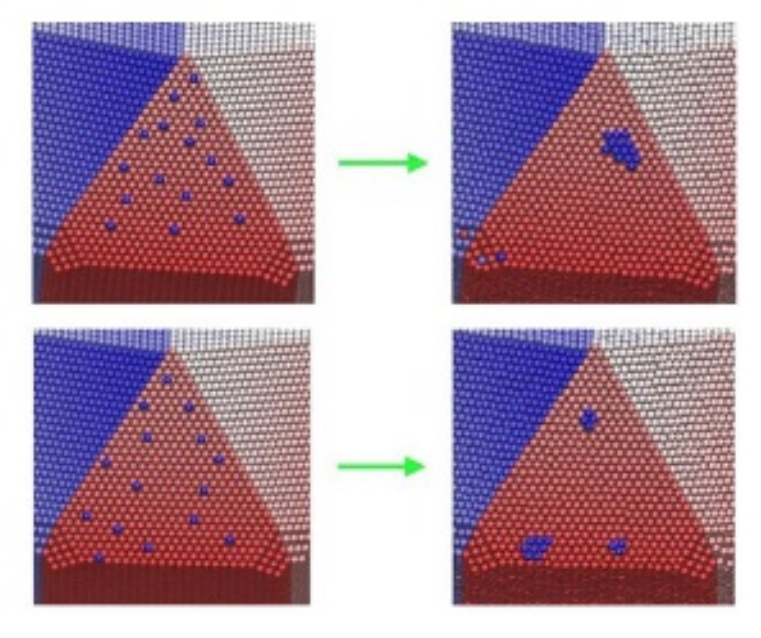
RESULTS AND DISCUSSION

Diffusion and Heterogeneous Aggregation on {111}

Our prior MD simulations showed that atoms diffuse rapidly on Ag(111), and form aggregates within ns, while atoms on Ag(100) diffuse relatively slowly and remain essentially isolated over the same time window.⁵⁷ Moreover, the heterogeneous strain distribution on the {111} end facets leads to the formation of aggregates that tend to be distributed near the {111}-{111}, {111}-{100}, and {111}-{110} facet edges, as shown in **Figure 3**. In these

PLEASE CITE THIS ARTICLE AS DOI: 10.1063/5.0146305

simulations, aggregation on {111} occurs more rapidly than {111}-{100} inter-facet diffusion, as we observed previously.⁵⁷ A new conclusion has emerged from the present study: We observed that small aggregates can possess significant mobility on Ag{111} – in particular, Ag dimers and trimers possess significant mobility, with trimers forming from dimers. We used the theory of absorbing Markov chains to quantify this mobility.



Snapshots from two, different, 4-ns MD simulations beginning with a random distribution of Ag atoms (left) on a {111} end facet of a nanocrystal seed with a width of 30 atoms on the {100} facet. The snapshots on the right depict the Ag aggregates at the end of 4 ns.

As shown in **Figure 4**, there are four states for a trimer on $\{111\}$. We denote I_1 and I₂, where all trimer atoms reside in the same cell (delineated in green in **Figure 4**), as initial states for trimer motion. T₁ and T₂ are states that trimers occupy as they transit between cells. In I₁ and T₂, atoms reside on fcc sites and on I₂ and T₁, atoms reside on hcp sites. Based on these states, the diffusion pathways among trimer cells are shown in Figure 5.

PLEASE CITE THIS ARTICLE AS DOI: 10.1063/5.0146305

I₁ I₂ T₁ T₂

Figure 4. Different trimer states on {111}. The green lines delineate trimer cells and the blue dots represent trimer atoms. States with the triangle pointing to the tip of the {111} end are marked with 1 and states with the triangle pointing to the {100}-{111} edge are marked with 2.

In **Figure 5**, the pertinent trimer cells are I, U, L, and D. Note there is also an R (right) diffusion pathway that is equivalent to the L (left) and that U and D are degenerate, so the trimer can diffuse in six different directions. As for the I cell in **Figure 4**, each of these cells can contain two different trimer orientations (U₁, U₂, L₁, L₂, D₁, and D₂). If trimer diffusion on the {111} facet was isotropic, we would only need to characterize motion between two cells. However, due to strain associated with the penta-twinned structure, transit rates from I to U, L, and D are slightly different. In fact, the diffusion barriers also depend on their location on the {111} facet – though this dependence is not greatly different from what we present here so these pathways are characteristic. In **Figure 5**, we see that the trimer can rotate between I₁ and I₂ and translate to U₁, U₂, L₁, L₂, D₁, and D₂. **Figure 6** shows a diagram of the pathways and the energy barriers to move between these states.

PLEASE CITE THIS ARTICLE AS DOI: 10.1063/5.0146305

Publishing Chemical Ph

Figure 5. Transitions between trimer cells (delineated by green lines) on $\{111\}$. Seven different pathways $(P_1 - P_7)$ are shown. I is the initial cell. As shown in **Figure 4**, we can have two different trimer conformations in $I - I_1$ and I_2 and we can have two different conformations for T, U, L, and D, as well. States T_1 and T_2 can be approached from different pathways, in which they have different barriers – hence the additional subscripts. P_4 and P_5 from I to U move the trimer closer to the penta-twinned tip and P_6 and P_7 from I to D move the trimer closer to the $\{111\}$ - $\{100\}$ interface. The blue dots represent the initial position of the trimer and the diffusion pathways are shown with yellow arrows.

We note that Shah *et al.* found similar mechanisms to us $(P1 - P4 \text{ in } \mathbf{Figure 5})$ in their study with an EAM potential⁷³ – though we found additional mechanisms P5-P7. The energy barriers that we find (cf., **Figure 6**) are similar to those found by Shah *et al.* but our barriers are slightly, but systematically higher. This could be because they studied diffusion on flat (unstrained) Ag(111) or because of differences in the EAM potentials used by us and them.

PLEASE CITE THIS ARTICLE AS DOI: 10.1063/5.0146305

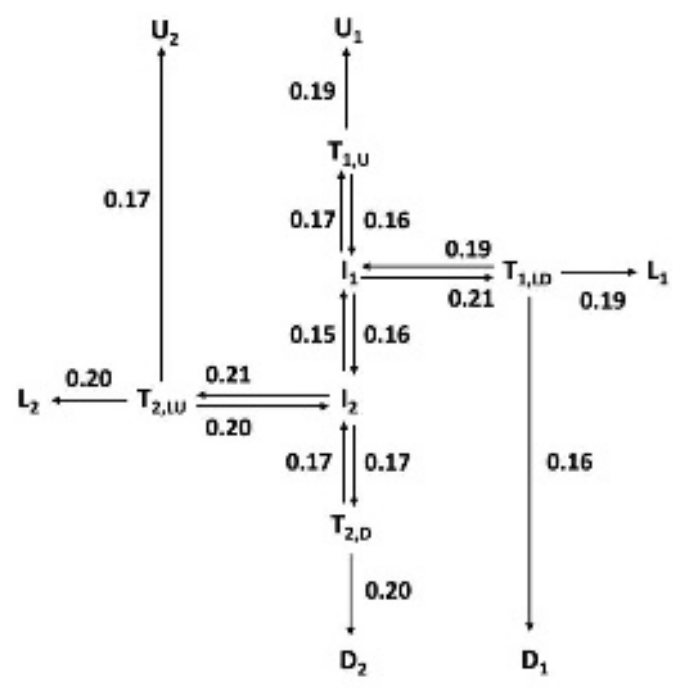


Figure 6. Forward and reverse energy barriers (in eV) for an Ag trimer to transit between the various states described in **Figures 4** and **5**.

We used the theory of absorbing Markov chains to calculate the rate to transit from I to L, U, and D. In this calculation, I_1 , I_2 , T_1 , and T_2 are transient states, while D_1 , D_2 , L_1 , L_2 , U_1 , and U_2 are absorbing states in Equations (6)-(10). We assumed I_1 and I_2 had equal occupation probabilities (0.5) initially and that T_1 and T_2 were initially vacant. The rates to transit between each pair of states i and j were given by the Arrhenius form of $r_{ij} = A \exp(-E_{ij}/kT)$ with $A = 10^{13}$ s⁻¹. From the net escape rate, given by Equation (9), and the probabilities of reaching the different possible absorbing states, given by Equation (10), we could determine the net rates for a trimer to diffuse in all directions at a fixed temperature. We obtained the overall energy barrier and pre-exponential factor for each process from Arhenius plots of these rates for different temperatures. These results indicated the trimer diffuses in the U and D directions with similar rates that are faster

PLEASE CITE THIS ARTICLE AS DOI: 10.1063/5.0146305

than the rates for the trimer to diffuse in the L (and R) directions. This calculation is presented in detail in the **Supplementary Information** and the results are included in Table 1.

Net Diffusion Rate from {111} to {100}

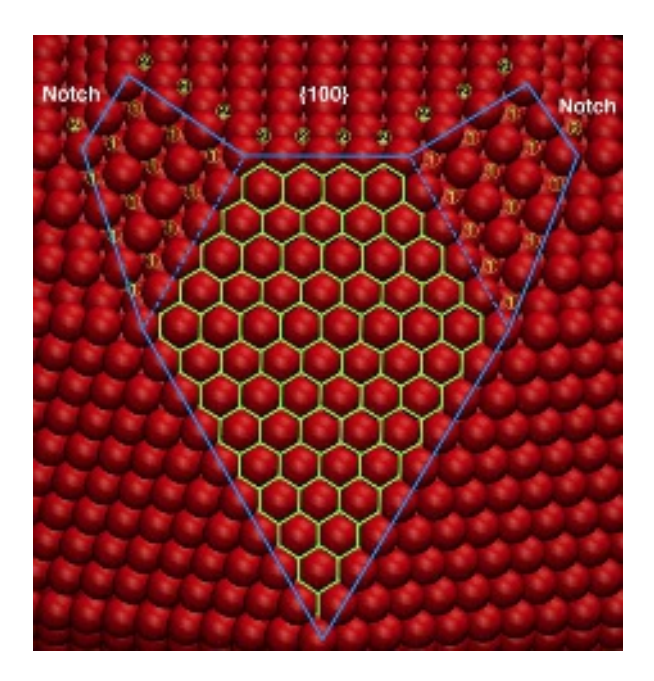


Figure 7. A map of the states involved in calculating $R_{\{111\}\to\{100\}}$. The green lines delineate trimer cells on {111}, 1 denotes sites on the {110} steps, 2 denotes absorbing states, and the complete cell is enclosed by blue lines.

Figure 7 shows a complete map of the states involved with diffusion on the {111} facet and diffusion between {111} and {100}. The transient states are trimer cells on {111}, outlined in green, and sites on {110}, marked with 1. The absorbing states, marked with 2, lie on the {100} facet and the {111} notch. Note that we include the {110} steps as part of the {111} facet. We employ reflecting boundary conditions to handle transitions

PLEASE CITE THIS ARTICLE AS DOI: 10.1063/5.0146305

Publishing Chemical

between trimer states in neighboring $\{111\}$ cells. To obtain $R_{\{111\}\to\{100\}}$ in Equations (1) and (2), we need to characterize diffusion between $\{111\}$ and $\{110\}$, on $\{110\}$, between $\{110\}$ and the $\{111\}$ notch, and between $\{111\}$ and $\{100\}$. The energy barriers and prefactors for these processes are included in **Table 1**.

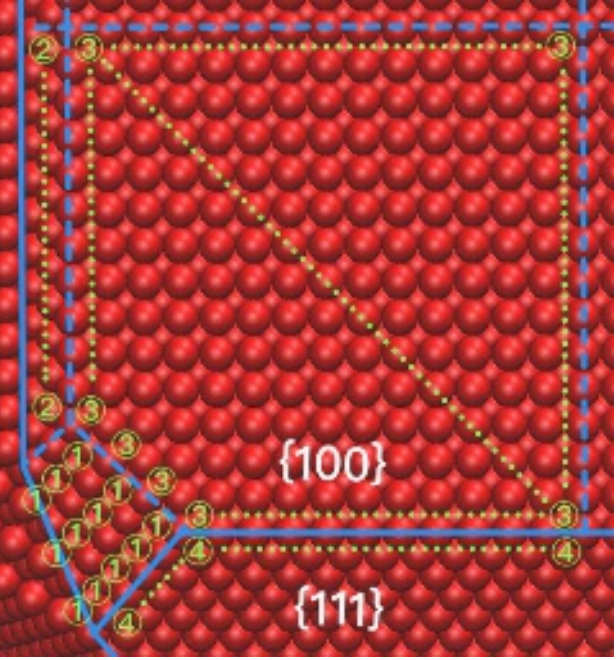


Figure 8. A map of the states involved in calculating $R_{\{100\}\to\{111\}}$. 1 denotes sites on the $\{110\}$ steps, 2 denotes sites in the $\{111\}$ notches, 3 denotes sites on $\{100\}$, 4 denotes absorbing states, and the complete cell is enclosed by the solid blue lines. Dotted lines are shown to avoid excessive delineation of states 2-4.

Figure 8 shows a complete map of the states involved in quantifying the diffusion rate from {100} to {111}. States 1, 2, and 3 in **Figure 8** are transient states and states marked 4 are absorbing states. A quarter of the {100} facet is used to represent the whole facet, based on symmetry, and we apply reflecting boundary coditions at the {100}-{100} and notch-notch cell boundaries. The {110} steps and the {111} notches are included as part

PLEASE CITE THIS ARTICLE AS DOI: 10.1063/5.0146305

of the $\{100\}$ facet. To obatin $R_{\{100\}\to\{111\}}$ in Equations (1) and (2), we need to characterize diffusion between $\{100\}$ and the $\{111\}$ notch, between $\{100\}$ and $\{111\}$, between $\{100\}$ and $\{110\}$, between the $\{111\}$ notch and $\{110\}$, and between $\{110\}$ and $\{111\}$. The energy barriers and prefactors for these processes are included in **Table 1**.

Key diffusion barriers

Table I. Key barriers (eV) and pre-exponential factors (s⁻¹) for diffusion processes on an uncapped Dh Ag surface.

Diffusion Process	Event	Forward / Reverse Barrier	Prefactor
Hopping on {100}	Parallel to (110)	0.51/0.51	10 ¹³
	Perpendicular to (110)	0.53/0.53	
Exchange Diffusion {100}→{111} notch	Single atom on {100}, Dimer in notch	0.62/0.76	
Exchange Diffusion	Parallel to (110)	0.39/0.72	
$\{100\} \rightarrow \{110\} \text{ step}$	Perpendicular to (110)	0.36/0.69	
On {110} step	Hopping along {110}	0.33/0.33	
	Exchange across {110}	0.31/0.31	
Exchange Diffusion From notch to step	Dimer in {111} notch, single atom on {110} step	0.30/0.31	
Exchange Diffusion {111}→{100}	Single Atom	0.41/0.67	
	Single atom on {100}, Trimer on {111}	0.57/0.16	
Exchange Diffusion $\{110\}$ step $\rightarrow \{111\}$	Single atom on {110}, Trimer on {111}	0.46/0.55	
Hopping along {111} notch	Dimer	0.21/0.21	
Trimer Diffusion	Parallel to {100}-{111} Edge	0.21/0.21	2.0 x 10 ¹²
	Perpendicular to {100}- {111} Edge	0.19/0.19	2.3 x 10 ¹²

The diffusion energy barriers in **Table 1** characterize hopping of atoms on top of the surfaces, as well as mechanisms in which atoms on top of the surface exchange with atoms in the surface. In our previous study,⁵⁷ we found that the diffusion unit in the notch is an Ag dimer

PLEASE CITE THIS ARTICLE AS DOI: 10.1063/5.0146305

and, as discussed above, the unit on {111} is a trimer. The barrier for a single Ag atom to diffuse from {111} to {100} is lower than the reverse barrier, which is not conducive for atom accumulation on {111} and nanowire growth. However, the inter-facet diffusion barrier for an Ag atom in a trimer to move from {111} to {100} is much higher than the barrier for an atom on {100} to join a dimer to make a trimer, which is reversed from the single-atom scenario.

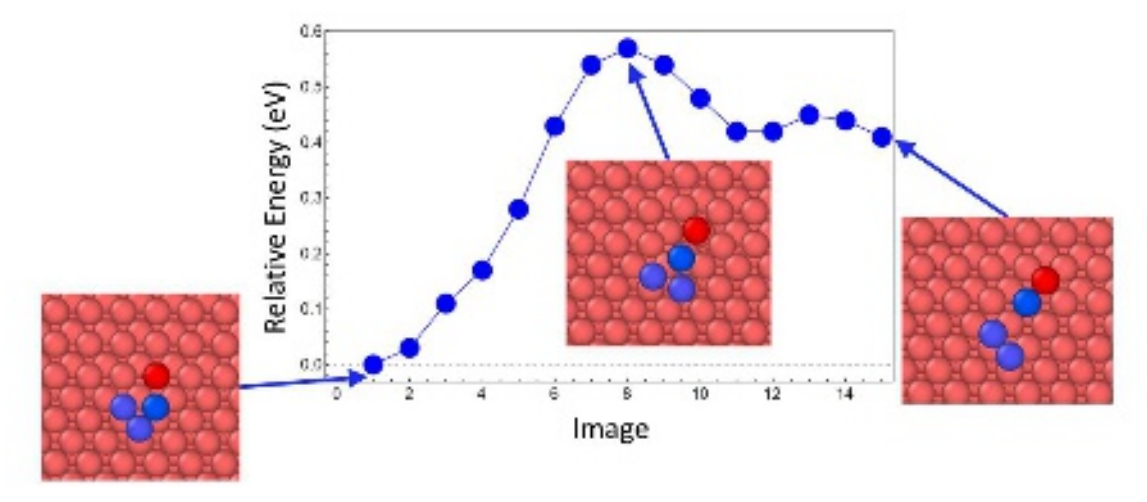


Figure 9. Mechanism by which an atom in an Ag trimer on Ag(111) (shown in blue) takes the place of a surface atom in the $\{111\}$ - $\{100\}$ interface (shown in red) and pushes the red interface atom onto Ag(100), resulting in a dimer on Ag(111) and an atom on Ag(100).

Figure 9 shows the mechanism for inter-facet diffusion of a trimer. Initially, an atom in a trimer on Ag(111) moves to take the position of a surface atom in the {111}-{100} interface. The initial trimer atom takes the place of the surface atom and pushes it up onto Ag(100). A similar scenario exists for motion between the {110} and {111} facets. Thus, aggregation close to the edges of the {111} facets, as we observe in **Figure 3**, facilitates Ag nanowire growth.

Predictions and Comparisons with Experiments

Our calculations proceed as follows: First, we create a seed crystal with fixed dimensions of the {100} width and the {100} length – the {100} width determines

the size of the {111} end facets. Subsequently, we calculate the MFPT for an atom to

After determining the facet on which accumulation will occur, we predict the aspect ratio of the final products to be the ratio of the length to the width achieved when the inter-facet diffusion rate on the facet without accumulation equals the deposition rate. For NW or NR products, accumulation occurs on {111} and three processes are important: deposition on {111}, deposition on {100} and diffusion from {100} to {111}. Hence, $G_{\{100\}}$ and $G_{\{111\}}$ in Equations (1) and (2) become

PLEASE CITE THIS ARTICLE AS DOI: 10.1063/5.0146305

 $G_{\{100\}} = R_{d,\{100\}} - R_{\{100\} \to \{111\}}$ (11)

and

$$G_{\{111\}} = R_{d,\{111\}} + R_{\{100\} \to \{111\}}$$
 (12)

We find $R_{d,\{100\}}\gg R_{d,\{111\}}$, so $R_{d,\{100\}}\approx R_{dep}$, $G_{\{111\}}$ is always positive, and $G_{\{100\}}$ could be either negative or positive. For negative $G_{\{100\}}$, we have $R_{\{100\} \to \{111\}} > R_{d,\{100\}}$, no accumulation occurs on {100}, and {100} will grow longer. When $G_{\{100\}}$ is positive, accumulation occurs on {100}, inter-facet diffusion from {100} to {111} is limited, and the NWs grow thicker. A similar scenario occurs for the growth of Dh, with accumulation on {100}. We estimate the final aspect ratios of the products (NW, NR, of Dh) as the dimensions obtained when either $G_{\{100\}}$ [using Equations (11)-13) above] or $G_{\{111\}}$ [using similar equations to (11)-(13) above] becomes zero.

Figure 10 shows the predicted aspect ratio for penta-twinned Ag products as a function of the initial {100} dimensions of a Dh seed. The purple region in **Figure 10** represents growth from seed sizes where $R_{111\rightarrow 100} > R_{100\rightarrow 111}$ initially and Dh products are predicted. In this region, the aspect ratio (the ratio of the total length to the diameter of the crystal) is 0.6~0.7. The seed sizes located on the boundary of the purple region have comparable inter-facet diffusion rates between {100} and {111}. In this case, the aspect ratios of the products are similar to the initial aspect ratios of the seeds, which are 0.8~1.0.

PLEASE CITE THIS ARTICLE AS DOI: 10.1063/5.0146305

Interestingly, the boundaries of the purple region in **Figure 10** are slightly wavy due to the discreteness of the seeds, which can only increase in size by integer numbers of atoms.

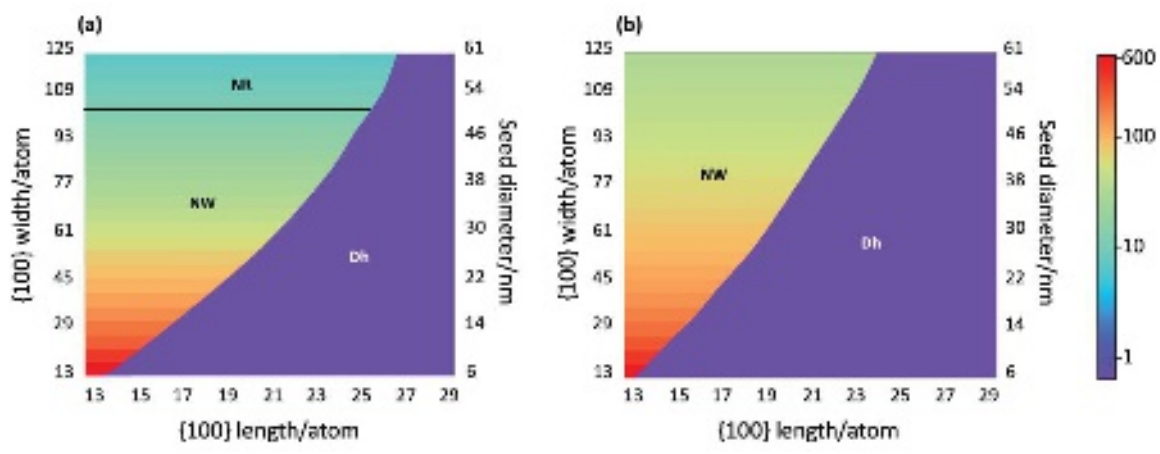


Figure 10. Contour plots of aspect ratio (ratio of total length to diameter) predictions as a function of the initial lengths and widths of Ag seeds at (a) 373 K and (b) 403 K. The scale bar denotes the aspect ratio of the final structure. Products with aspect ratios greater than 1 and 10 or less are categorized as NR.

The left regions of Figure 10, with colors ranging from red to blue, occur for seed sizes with $R_{\{100\}\rightarrow\{111\}} > R_{\{111\}\rightarrow\{100\}}$, such that the seeds will grow longer. In **Figure 10**, we see that the final aspect ratio of the products depends only on the {100} width, but the range of seed lengths over which NW or NR products occur increases with increasing {100} width. This is because once a NW or NR begins to grow, it increases its length through other seed lengths until it can no longer continue to grow. It is evident that NWs with the highest aspect ratios occur for seeds with the smallest diameters, consistent with the fact that $R_{\{100\} \to \{111\}}$ has the highest values for the smallest facets. Comparing **Figures 10(a)** and 10(b), we see that increasing the temperature improves the aspect ratio, which is consistent with faster diffusion on the time scale of deposition. Here, it is important to note that we only consider the effect of temperature on surface diffusion and that temperature

PLEASE CITE THIS ARTICLE AS DOI: 10.1063/5.0146305

can affect other aspects of an experimental synthesis, such as the reduction rate, which is often equated to the deposition rate.

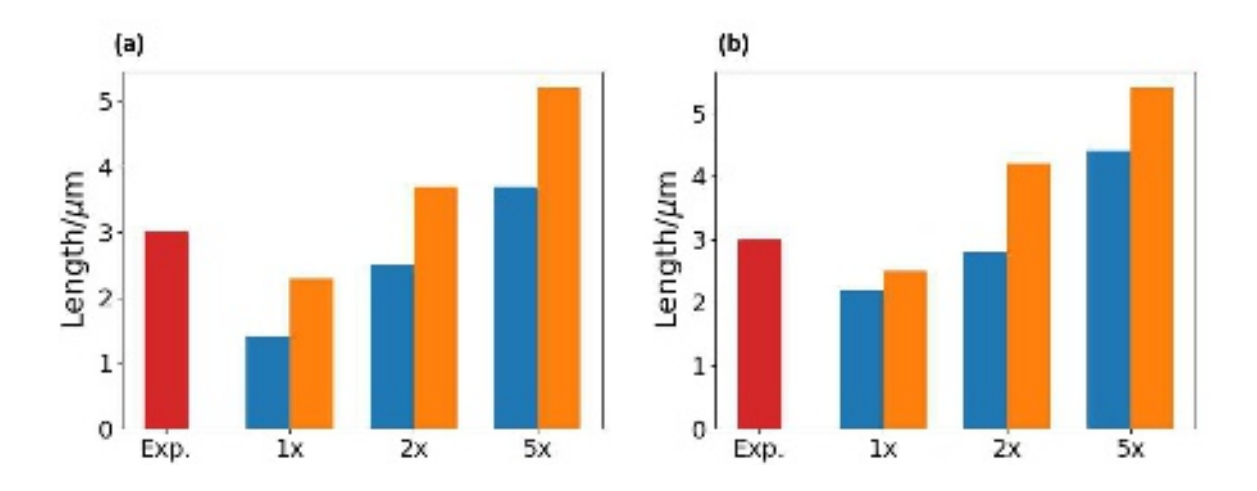


Figure 11. Comparisons between nanowire lengths predicted by our model and (a) Caswell's work, (b) Yang's work for nanowires of the same diameters as in experiment. The red columns are the average length reported in the experiments. The blue and the orange columns are the minimum and maximum length predictions for each experiment, based on the range of experimentally reported diameters, with inter-facet transit rates of $R_{100\to111}$ (1x), $2R_{100\to111}$ (2x), and $5R_{100\to111}$ (5x), as discussed in the text.

Figure 11 shows a comparison of predicted nanowire lengths from our model to two experiments. Caswell *et al.* synthesized penta-twinned Ag nanowires at 373K with AgNO₃ and trisodium citrate in water, in the absence of a surfactant, and without an externally added seed. The diameters of the wires were 35 ± 6 nm and the average length was $3 \mu m$. From the experimental data, the deposition rate was $\sim 10^3 s^{-1}$. For wires with diameters ranging from 29 to 41 nm, we predict lengths ranging from 2.3 to 1.4 μm , as shown in Figure 11(a) (1x).

This is the author's peer reviewed, accepted manuscript. However, the online version of record will be different from this version once it has been copyedited and typeset.

PLEASE CITE THIS ARTICLE AS DOI: 10.1063/5.0146305

citrate without any external seeds. 14 The average diameter was 53 \pm 4 nm and the length was 3 µm on average. The deposition rate was $\sim 10^3 s^{-1}$ based on the experimental data. As we see in **Figure 11(b)**, our predicted lengths for 1x are somewhat shorter than experiment, the lengths for 2x bracket experiment, and the lengths for 5x exceed experiment.

Conclusions

Using the theory of absorbing Markov chains to account for the growth of pentatwinned Dh seeds via atom deposition and surface diffusion, we predicted the formation of various types of products (Dh, NR, and NW) from Dh Ag seeds. We showed that the type of product depends on the morphology of the seed and that small differences between various seed morphologies can lead to significantly different products. For the case of uncapped Dh seeds, we compared predictions from our model to NW morphologies obtained in two different experiments and obtained favorable agreement.

PLEASE CITE THIS ARTICLE AS DOI: 10.1063/5.0146305

Based on this model, we expect NWs to form with higher aspect ratios at higher temperatures – with the caveat that we only consider the temperature dependence of surface diffusion. Also implicit in the model is the fact that we would predict higher aspect ratios with lower deposition rates because NWs would grow longer with less time between successive depositions. This prediction is at odds with a recent experimental study of *capped* Ag nanowires, where they grew longer NW with higher deposition rates.⁷⁴ In that study, they attributed this type of growth to limited diffusion from the NW end to the side with a high deposition rate and more significant diffusion with a low deposition rate. It would be possible to extend our model to capped surfaces (we did this previously,⁵⁸ but did not consider the influence of the deposition rate) to investigate these phenomena. We also note that it would also be possible to determine the effects of solvent and capping molecules on deposition and surface diffusion, as we did previously for deposition.⁷⁵ Such efforts would extend the range of predictions for this model.

Supplementary Information

An example of calculating the mean first-passage time for trimer diffusion on Ag(111) is included in the **Supplementary Information.**

Acknowledgements

This work was funded by the National Science Foundation, Grant OAC-1835607.

References

1. S. Ge, Z. Cai, H. Zhang, L. He, P. Wang, L. Zhang, and Y. Fang, Nanotechnology **32**, 465604 (2021).

- This is the author's peer reviewed, accepted manuscript. However, the online version of record will be different from this version once it has been copyedited and typeset.

 PLEASE CITE THIS ARTICLE AS DOI: 10.1063/5.0146305
- 2. D. A. Moraes, J. B. Souza Junior, F. F. Ferreira, N. V. V. Mogili, and L. C. Varanda, Nanoscale **12**, 13316 (2020).
- 3. V. Mastronardi, G. Udayan, G. Cibecchini, R. Brescia, K. A. Fichthorn, P. P. Pompa, and M. Moglianetti, ACS Appl. Mater. Interfaces **12**, 49935 (2020).
- 4. Y. Li, Z. Y. Fan, X. M. Yuan, H. W. Yang, Y. X. Li, and C. Wang, Mater. Lett. **274**, 128029 (2020).
- 5. R. Takahata, and T. Tsukuda, Chem. Lett. **48**, 906 (2019).
- 6. M. J. Kim, S. Alvarez, T. Y. Yan, V. Tadepalli, K. A. Fichthorn, and B. J. Wiley, Chem. Mater. 30, 2809 (2018).
- 7. M. Luo, A. Ruditskiy, H. C. Peng, J. Tao, L. Figueroa-Cosme, Z. K. He, and Y. N. Xia, Adv. Funct. Mater. **26**, 1209 (2016).
- 8. R. R. da Silva, M. Yang, S. I. Choi, M. Chi, M. Luo, C. Zhang, Z. Y. Li, P. H. Camargo, S. J. Ribeiro, and Y. Xia, ACS Nano **10**, 7892 (2016).
- 9. S. Ye, I. E. Stewart, Z. Chen, B. Li, A. R. Rathmell, and B. J. Wiley, Acc. Chem. Res. **49**, 442 (2016).
- 10. M. Tsuji, M. Hashimoto, Y. Nishizawa, and T. Tsuji, Mater. Lett. **58**, 2326 (2004).
- 11. Z. Niu, F. Cui, E. Kuttner, C. Xie, H. Chen, Y. Sun, A. Dehestani, K. Schierle-Arndt, and P. Yang, Nano Lett. **18**, 5329 (2018).
- 12. K. K. Caswell, C. M. Bender, and C. J. Murphy, Nano Lett. 3, 667 (2003).
- 13. M. J. Kim, S. Alvarez, Z. Chen, K. A. Fichthorn, and B. J. Wiley, J. Am. Chem. Soc. **140**, 14740 (2018).
- 14. Z. Yang, H. Qian, H. Chen, and J. N. Anker, J Colloid Interface Sci **352**, 285 (2010).
- 15. V. Kitaev, and T. Subedi, Chem. Commun. **53**, 6444 (2017).
- 16. M. Brown, and B. J. Wiley, Chem. Mater. **32**, 6410 (2020).
- 17. S. E. Lohse, and C. J. Murphy, Chem. Mater. **25**, 1250 (2013).
- 18. W. M. Tong, M. J. Walsh, P. Mulvaney, J. Etheridge, and A. M. Funston, J. Phys. Chem. C **121**, 3549 (2017).
- 19. S. Zhou, M. Zhao, T. H. Yang, and Y. N. Xia, Mater. Today **22**, 108 (2019).
- 20. X. Ma, F. Lin, X. Chen, and C. Jin, ACS Nano 14, 9594 (2020).

- This is the author's peer reviewed, accepted manuscript. However, the online version of record will be different from this version once it has been copyedited and typeset.

 PLEASE CITE THIS ARTICLE AS DOI: 10.1063/5.0146305
- 21. T. H. Chow, N. Li, X. Bai, X. Zhuo, L. Shao, and J. Wang, Acc. Chem. Res. **52**, 2136 (2019).
- 22. M. Song, Z. Wu, N. Lu, and D. Li, Chem. Mater. **31**, 842 (2019).
- 23. H. Huang, Y. Wang, A. Ruditskiy, H. C. Peng, X. Zhao, L. Zhang, J. Liu, Z. Ye, and Y. Xia, ACS Nano 8, 7041 (2014).
- 24. X. Zheng, X. Zhao, D. Guo, B. Tang, S. Xu, B. Zhao, W. Xu, and J. R. Lombardi, Langmuir **25**, 3802 (2009).
- 25. L. C. Yang, Y. S. Lai, C. M. Tsai, Y. T. Kong, C. I. Lee, and C. L. Huang, J. Phys. Chem. C **116**, 24292 (2012).
- 26. G. Casillas, J. J. Velazquez-Salazar, and M. Jose-Yacaman, J. Phys. Chem. C 116, 8844 (2012).
- 27. Y. Xia, Y. Xiong, B. Lim, and S. E. Skrabalak, Angew. Chem., Int. Ed. Engl. **48**, 60 (2009).
- 28. M. J. Kim, M. A. Cruz, F. Yang, and B. J. Wiley, Curr. Opin. Electrochem. **16**, 19 (2019).
- 29. M. L. R. Liman, M. T. Islam, and M. M. Hossain, Adv. Electron. Mater. **8**, (2022).
- 30. Z. Li, X. Xu, X. Sheng, P. Lin, J. Tang, L. Pan, Y. V. Kaneti, T. Yang, and Y. Yamauchi, ACS Nano, (2021).
- 31. H. Jia, X. Yang, Q. Q. Kong, L. J. Xie, Q. G. Guo, G. Song, L. L. Liang, J. P. Chen, Y. Li, and C. M. Chen, J. Mater. Chem. A **9**, 1180 (2021).
- 32. S. Y. Huang, Y. N. Liu, M. Jafari, M. Siaj, H. N. Wang, S. Y. Xiao, and D. L. Ma, Adv. Funct. Mater. **31**, (2021).
- 33. M. A. Shinde, and H. Kim, Synth. Met. **254**, 97 (2019).
- 34. K. Mallikarjuna, and H. Kim, ACS Appl. Mater. Interfaces 11, 1969 (2019).
- 35. Z. G. Guo, C. Sun, J. Zhao, Z. S. Cai, and F. Y. Ge, Adv. Mater. Interfaces **8**, (2021).
- 36. S.-S. Chee, H. Kim, M. Son, and M.-H. Ham, Electron. Mater. Lett. **16**, 404 (2020).
- 37. Y. W. Zhu, Y. J. Deng, P. Y. Yi, L. F. Peng, X. M. Lai, and Z. Q. Lin, Adv. Mater. Technol. **4**, (2019).

This is the author's peer reviewed, accepted manuscript. However, the online version of record will be different from this version once it has been copyedited and typeset.

PLEASE CITE THIS ARTICLE AS DOI: 10.1063/5.0146305

- P. Won, J. J. Park, T. Lee, I. Ha, S. Han, M. Choi, J. Lee, S. Hong, K. J. Cho, and S. H. Ko, Nano Lett. 19, 6087 (2019).
- 39. J. Jung, H. Cho, R. Yuksel, D. Kim, H. Lee, J. Kwon, P. Lee, J. Yeo, S. Hong, H. E. Unalan, S. Han, and S. H. Ko, Nanoscale **11**, 20356 (2019).
- 40. C. R. Chen, H. Qin, H. P. Cong, and S. H. Yu, Adv. Mater. **31**, e1900573 (2019).
- 41. N. S. Abadeer, and C. J. Murphy, J. Phys. Chem. C **120**, 4691 (2016).
- 42. A. M. Alkilany, L. B. Thompson, S. P. Boulos, P. N. Sisco, and C. J. Murphy, Adv. Drug Deliv. Rev. **64**, 190 (2012).
- 43. S. I. Choi, J. A. Herron, J. Scaranto, H. W. Huang, Y. Wang, X. H. Xia, T. Lv, J. H. Park, H. C. Peng, M. Mavrikakis, and Y. N. Xia, ChemCatChem 7, 2077 (2015).
- 44. K. Kołątaj, J. Krajczewski, and A. Kudelski, J. Phys. Chem. C **121**, 12383 (2017).
- 45. Y. H. Chien, C. C. Huang, S. W. Wang, and C. S. Yeh, Green Chem. **13**, 1162 (2011).
- 46. C. L. Cleveland, and U. Landman, J. Chem. Phys. **94**, 7376 (1991).
- 47. F. Baletto, R. Ferrando, A. Fortunelli, F. Montalenti, and C. Mottet, J. Chem. Phys. **116**, 3856 (2002).
- 48. J. M. Rahm, and P. Erhart, Nano Lett. **17**, 5775 (2017).
- 49. K. A. Fichthorn, and T. Yan, J. Phys. Chem. C **125**, 3668 (2021).
- 50. K. A. Fichthorn, Chem. Rev., doi: 10.1021/acs.chemrev.2c00831 (2023).
- 51. M. Tsuji, M. Ogino, R. Matsuo, H. Kumagae, S. Hikino, T. Kim, and S.-H. Yoon, Cryst. Growth Des. **10**, 296 (2009).
- 52. S. E. H. Murph, C. J. Murphy, A. Leach, and K. Gall, Cryst. Growth Des. **15**, 1968 (2015).
- 53. M. Song, G. Zhou, N. Lu, J. Lee, E. Nakouzi, H. Wang, and D. Li, Science **367**, 40 (2020).
- 54. J. S. Du, W. Zhou, S. M. Rupich, and C. A. Mirkin, Angew. Chem., Int. Ed. Engl. **60**, 6858 (2021).
- 55. D. Li, Q. Chen, J. Chun, K. A. Fichthorn, J. J. De Yoreo, and H. Zheng, Chem. Rev., (2022).

PLEASE CITE THIS ARTICLE AS DOI: 10.1063/5.0146305

56. E. Y. El Koraychy, C. Roncaglia, D. Nelli, M. Cerbelaud, and R. Ferrando, Nanoscale Horiz 7, 883 (2022). 57. X. Qi, Z. Chen, T. Yan, and K. A. Fichthorn, ACS Nano 13, 4647 (2019). 58. J. Kim, J. Cui, and K. A. Fichthorn, ACS Nano 15, 18279 (2021).

- 59. K. A. Fichthorn, Z. Chen, Z. Chen, R. M. Rioux, M. J. Kim, and B. J. Wiley, Langmuir **37**, 4419 (2021).
- 60. A. A. Chernov, Sov. Phys. Crystallog. **7**, 728 (1963).
- 61. S. B. Gadewar, and M. F. Doherty, J. Cryst. Growth **267**, 239 (2004).
- 62. K. A. Fichthorn, and W. H. Weinberg, J. Chem. Phys. **95**, 1090 (1991).
- 63. J. G. Kemeny, and J. L. Snell, *Finite Markov Chains* (Van Nostrand, Princeton, NJ USA, 1976), Undergraduate Texts in Mathematics,
- 64. M. Iosifescu, *Finite Markov Processes and Their Applications* (Dover Publications, Inc., Mineola, New York, 1980),
- 65. M. A. Novotny, Phys. Rev. Lett. **74**, 1 (1995).
- 66. B. Puchala, M. L. Falk, and K. Garikipati, J. Chem. Phys. **132**, 134104 (2010).
- 67. K. A. Fichthorn, and Y. Lin, J. Chem. Phys. **138**, 164104 (2013).
- 68. J. Kim, and K. A. Fichthorn, Faraday Discuss. **235**, 273 (2022).
- 69. L. D. Marks, Philos. Mag. A **49**, 81 (1984).
- 70. P. L. Williams, Y. Mishin, and J. C. Hamilton, Modell. Simul. Mater. Sci. Eng. **14**, 817 (2006).
- 71. S. Plimpton, J. Comput. Phys. **117**, 1 (1995).
- 72. G. Henkelman, B. P. Uberuaga, and H. Jonsson, J. Chem. Phys. **113**, 9901 (2000).
- 73. S. I. Shah, G. Nandipati, A. Karim, and T. S. Rahman, J. Phys. Condens. Matter **28**, 025001 (2016).
- 74. D. Hu, F. Qin, J. Liu, H. Lai, T. Tan, C. Li, and C. Wang, ACS Appl. Nano Mater. **5**, 957 (2022).
- 75. X. Qi, T. Balankura, Y. Zhou, and K. A. Fichthorn, Nano Lett. **15**, 7711 (2015).

ACCEPTED MANUSCRIPT

The Journal of Chemical Physics



This is the author's peer reviewed, accepted manuscript. However, the online version of record will be different from this version once it has been copyedited and typeset.

PLEASE CITE THIS ARTICLE AS DOI: 10.1063/5.0146305

